Study on the limits of all-optical time domain demultiplexing using cross absorption modulation in an electroabsorption modulator

Study on the limits of all-optical time-domain demultiplexing using cross-absorption modulation in an electroabsorption modulator

E.J.M. Verdurmen, Y. Liu, G.D. Khoe and H. de Waardt

Abstract: A theoretical and experimental assessment of the performance of an all-optical demultiplexer based on cross-absorption modulation in an electroabsorption modulator is presented. Simulations are described for demultiplexing from 160 Gbit/s to a 40 or 10 Gbit/s base rate. Experimental results are presented for demultiplexing to a base rate of 10 Gbit/s from an optical time-domain multiplexing rate of 80 with a bit error rate (BER) $<10^{-9}$ and 160 Gbit/s with a BER $\simeq 10^{-7}$.

1 Introduction

Optical time-domain multiplexed (OTDM) systems are a propitious way to increase the capacity of optical systems, without increasing the cost of using high-speed electronics [1]. A further increase in the channel speed to 160 Gbit/s or beyond will lead to a reduction in cost, because the number of required light sources is reduced and network management is simplified compared to a wavelength division multiplexing (WDM) system. The channel rates that are achieved with OTDM exceed the limit of current available electronics. As a consequence all-optical techniques to handle such high channel rates are an interesting topic of research. One key functionality in future OTDM networks will be the extraction of a signal channel at the base rate from a multiplexed high bit rate data stream, which will enable the down conversion from ultra-high bit rates to a base rate of 40 or 10 Gbit/s.

All-optical fibre-based demultiplexing techniques have been demonstrated by using cross-phase modulation [2] or four-wave mixing (FWM) [3] in a highly non-linear fibre (HNLF). Another attractive option for demultiplexing is with active components, i.e. semiconductor optical amplifiers (SOAs). Demultiplexing with SOAs can be based on FWM [4]. SOAs can also be placed in an interferometric structure such as the semiconductor laser amplifier in a loop mirror [5], the terahertz optical asymmetric demultiplexer [6] or the gain transparent ultrafast non-linear interferometer [7, 8]. However, these schemes require complex configurations. Using only a single electroabsorption modulator (EAM) is promising due to the possibility of monolithic integration, with a simple waveguide structure [9] or a travelling wave design as in [10] and [11].

The EAM has been shown to be a key component in realising high-speed OTDM systems. The functionalities include pulse generation [12], modulation, wavelength conversion [13], clock recovery [14–16] and OTDM demultiplexing [9, 17, 18]. Recent efforts on the integration of mode-locked lasers (MLLs) have lead to very interesting options for all-optical clock recovery [19]. The next integration step would be to integrate an optically controlled gate together with the MLL to create an all-optical integrated OTDM demultiplexer. An EAM could serve as such an optically activated gate by exploiting the cross-absorption modulation (XAM) mechanism. We present a detailed investigation of the potential of using a commercially available multiple quantum well-EAM as a key element in an optically pumped drop configuration. XAM has been investigated before [20], but we will compare XAM with a concept that utilises the cross-polarisation rotation (XPR) in addition to the XAM in the EAM. The injected high-intensity pump signal saturates the EAM, which leads to XAM, but it also introduces additional birefringence in the EAM. This additional birefringence leads to a rotation of the polarisation (XPR). The XPR + XAM can improve the extinction ratio compared to the use of XAM only. Theoretical assessment of the XAM effect in the EAM has been investigated by modelling [21]. The purpose of the currently presented model is to investigate the behaviour of the EAM in a quantitative matter. This model is experimentally verified and the limitations of the commercially available EAM are tested.

2 Operation principle

2.1 XAM

The operation principle is schematically shown in Fig. 1. XAM in an EAM occurs when two beams, of which at least one has a high power level, are launched co-propagating or counter-propagating into the EAM. Regarding all-optical demultiplexing these two signals can be addressed as the OTDM signal and the clock signal. The aim of the clock is to generate a switching window to gate the desired OTDM channel. By the absorption of the clock signal in the active region of the EAM, carriers will be generated. The increase in the number of carriers leads to a reduction in the absorption coefficient, due to screening of the electric field imposed on the device and band-filling (absorption saturation). Hence, the temporary reduction of the absorption

IEE Proceedings online no. 20050026

doi:10.1049/ip-opt:20050026

Paper first received 18th March and in revised form 24th August 2005

The authors are with the COBRA Research Institute, Eindhoven University of Technology, Eindhoven, The Netherlands

E-mail: e.j.m.verdurmen@tue.nl

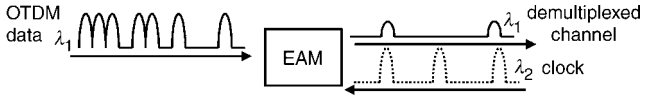

Fig. 1 *Principle of XAM with a counter-propagating clock signal*

coefficient allows one of the OTDM channels to pass through the EAM with a reduced absorption. The width of the created switching window depends on how fast the carriers can be swept out of the active region, which depends on the fixed DC reverse bias voltage and the details of the design.

2.2 XPR

The operation principle of XPR is schematically shown in Fig. 2. The concept of XPR in an EAM is used to increase the already operating XAM-effect by utilising the rotation of the polarisation. The OTDM data input is fed into the EAM counter-propagating to the clock signal. Injecting a high-intensity clock signal reduces the absorption coefficient of the EAM. A change in the absorption coefficient means a change in the refractive index, since they are related through the Kramers-Kronig equation. The injected clock signal also induces additional birefringence in the EAM, which causes the TE and the TM mode of the OTDM signal to experience a different refractive index change, resulting in a rotation of the polarisation [22]. The first polarisation controller (PC_1) is used to adjust the polarisation of the input signal to be approximately 45° to the orientation of the EAM layers. The polarisation of the clock signal is controlled by PC_3. The high-intensity clock signal at a different (or the same) wavelength as the OTDM signal saturates the EAM. The output of the EAM is sent to the polarisation beam splitter (PBS) via the circulator. The polarisation controller PC_2 is used to adjust the polarisation in such a way that the PBS will block the OTDM signal in the case where no clock signal is present in the EAM. On the other hand part of the signal will be allowed to pass through the PBS in the presence of a clock-pulse inside the EAM, as the polarisation is rotated. The high-intensity clock signal inside the EAM also induces XAM. The combination of XPR and XAM both work in the same direction and improves the extinction ratio at the output.

3 Model

To model the absorption dynamics of the EAM, we compute the well carrier densities, well carrier temperatures and also the photon density at every point inside the EAM, similar to the model presented in [23]. The parameters used in the simulations are listed in Table 1. The Fermi levels and temperatures of the carriers in the valence and conduction

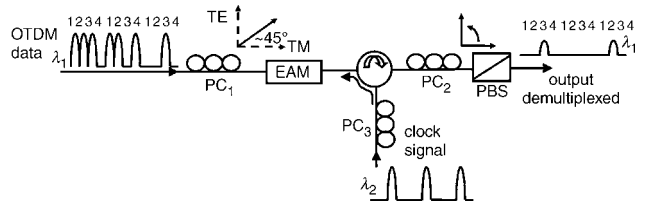

Fig. 2 *Principle of demultiplexing using XPR in a polarisation sensitive EAM, PC: polarisation controller, PBS: polarisation beam splitter*

Table 1: Simulation parameters

Carrier density at transparency N_{tr}, 1/m	1×10^{24}
Internal losses α_{int}, 1/m	4×10^{2}
Confinement factor, Γ	0.285
Group refractive index, n_g	3
Sweep-out time at zero carrier density τ_0, s	8×10^{-2}
Sweep-out time at transparency density τ_{tr}, s	25×10^{-12}
Effective area of active region [m^2] A_{eff}, m^2	3.6×10^{-13}
Absorption suppression [m^{-3}] ε_{supp}, $1/m^3$	2×10^{-24}
Unsaturated absorption [m^{-1}] α_0, 1/m	1.3×10^{5}
Carrier energy relaxation time [s] τ_{uc}, τ_{uv}, s	1×10^{-12}
Bandgap energy of InGaAsP E_{gap}	0.7992
Electron mass m_e, kg	9.1×10^{-31}
Mass of holes in the valence band m_v	$0.45m_e$
Mass of electrons in the conduction band m_c	$0.046m_e$

band are given by the balance equations for carriers and their energy in the absorbing region. The absorption coefficient also takes into account both spectral-hole burning (SHB) and carrier heating/cooling. Instead of using a field dependency in the Fermi distribution and the energy density, we use a simple carrier-density sweep-out model [24] that assumes a reverse bias voltage to put the EAM in the absorption regime. This sweep-out model describes the slowing down of the sweep-out time at high carrier densities. This is not a real physical model but is used to describe the behaviour of the sweep-out time in a phenomenological way. We have implemented this simplified relation for the sweep-out time in which the variation is dependent on the carrier density. The sweep-out time varies from 8 ps at low densities to 25 ps at transparency, based on the results in [24]. The complex pulse amplitudes $A(z, t)$ are slowly varying functions of z and t, and satisfy:

$$\left(\frac{\partial}{\partial z}+\frac{1}{v_g}\frac{\partial}{\partial t}\right)A(z,t) = -\frac{1}{2}(\Gamma\alpha(z,t)+\alpha_{int})A(z,t) \qquad (1)$$

where v_g is the group velocity, Γ is the confinement factor, α_{int} represents the internal loss coefficient and $\alpha(z, t)$ is the absorption coefficient. The pulse amplitude can be written as:

$$A(z,t) = \sqrt{S(z,t)}\, e^{j\phi(z,t)} \qquad (2)$$

where S is the photon density and $\varphi(z, t)$ is the phase of the light. Equation (1) leads to the following expression for the photon density in the active region, after transforming to the shifted time frame $t' = t - z/v_g$:

$$\frac{\partial S(z,t')}{\partial z} = -(\Gamma\alpha(z,t)+\alpha_{int})S(z,t') \qquad (3)$$

The absorption coefficient is calculated as a function of the well carrier densities, and takes into account both SHB and carrier heating/cooling. By not describing the field, electro-absorption effects are not included. Therefore, band-filling only induces the absorption changes. The absorption coefficient is expressed as:

$$\alpha = \alpha(z,t) = \frac{\alpha_0}{1+\varepsilon_{sup}S(z,t)}(1 - f_c(\varepsilon_{F_c}, E_c^0, T_c) - f_v(\varepsilon_{F_v}, E_v^0, T_v)) \qquad (4)$$

where α_0 is the unsaturated absorption coefficient, and f_c and f_v are the Fermi distributions characterised by the Fermi

levels ε_{F_i}, temperatures T_i and kinetic energy of the generated carriers E_i^0 [23], where $i = c, v$ refers to the conduction and valence band respectively. The term ε_{sup} is the absorption suppression factor due to SHB. The equations that describe the dynamics of the Fermi levels and the temperature are given by the balance equations for carriers and their energy in the absorbing region:

$$\frac{\partial n(z,t)}{\partial t} = -\alpha(z,t) \times v_g \times \Gamma \times S(z,t) - \frac{n(z,t) - n_{eq}}{\tau_{so}(n)} \quad (5)$$

$$\frac{\partial p(z,t)}{\partial t} = -\alpha(z,t) \times v_g \times \Gamma \times S(z,t) - \frac{p(z,t) - p_{eq}}{\tau_{so}(p)} \quad (6)$$

The balance equation for the energy density in the absorbing region is:

$$\frac{\partial u_i(z,t)}{\partial t} = S(z,t) \times \alpha(z,t) \times v_g \times E_i^0 - \frac{u_i - u_{Li}}{\tau_{ui}} - \frac{u_i}{\tau_{so}} \quad (7)$$

The variables n and p represent the local electron and hole densities, n_{eq} and p_{eq} are the local electron and hole densities in equilibrium, E_i^0 is the energy of the generated electrons ($i = c$) or holes ($i = v$) and τ_{ui} represents the energy relaxation time. The energy of electrons (holes) relaxes to the energy at lattice temperature: u_{Li}. In quantum well (QW) absorbers the photo-generated carriers are confined in the QW in the direction of the external field, so the field will not heat the carriers in the QW. Therefore, we may neglect the influence of the field on carrier temperature dynamics. The carrier density (n_i, $i = c, v$) and the energy density (u_i, $i = c, v$) can be described as:

$$n_i = N_i \times F_{1/2}\left[\frac{\varepsilon_{F_i}}{k_B T_i}\right] \quad (8)$$

$$u_i = \frac{3}{2} k_B \times T_i \times N_i \times F_{3/2}\left[\frac{\varepsilon_{F_i}}{k_B T_i}\right] \quad (9)$$

where $F_{1/2}$ and $F_{3/2}$ are the Fermi-Dirac integrals of the order $1/2$ and respectively $3/2$. N_i ($i = c, v$) is the effective density of states:

$$N_i = 2\left(\frac{m_i k_B T_i}{2\pi\hbar^2}\right)^{3/2} \quad (10)$$

More details about the model are described in [21].

The above-described model is used to simulate the demultiplexing of a 10 or 40 Gbit/s channel out of a 160 Gbit/s OTDM signal. An incoming 160 Gbit/s signal at $\lambda_1 = 1550$ nm and a 10 or 40 GHz optical clock signal at $\lambda_2 = 1540$ nm are injected into the EAM. First the switching window is investigated by analysing a continuous wave (CW) at $\lambda_1 = 1550$ nm signal co-propagating with a $\lambda_2 = 1540$ nm clock signal. The incremental step in the length of the EAM in the simulations $dz = 5$ μm. Figure 3 shows the switching windows for three different clock pulses. The power of the CW is 0 dBm. The energy of the clock pulses is 1.1 pJ, corresponding to a 10.5 dBm average power for the 10 GHz and 16.5 dBm average power for a 40 GHz clock signal. The clock pulses are respectively 1, 2 and 3 ps at full-width-half-maximum (FWHM). The corresponding switching windows are 1.8, 4.6 and 7 ps FWHM. We can deduce from Fig. 3 that the switching window becomes smaller when using shorter clock pulses. The disadvantage of the switching windows from Fig. 3 is the large tail, which complicates the suppression of the adjacent channel. The tail originates from the carrier sweep-out time, which limits the recovery speed of the absorption. An example of an eye-diagram of a demultiplexed signal is shown in Fig. 4. The clock signal is 40 GHz and the power of the pulse is 1.6 pJ. This power is not high enough to create a high contrast gate for the targeted channel. An increased saturation of the absorption is required for an increased contrast ratio between the targeted channel and the adjacent channels. By increasing the power of the clock signal, the saturation of the absorption is increased and the targeted channel is less absorbed, resulting in a higher contrast of the switching gate leading to a higher suppression ratio of the non-targeted channels. The relation between the channel suppression ratio and the power of the clock signal is shown in Fig. 5 for co- and counter-propagating operation. The length of the active region in this simulation is chosen to be 150 μm and the pulse width of the clock signal is 1.7 ps, corresponding to the actual pulse width in the experiments. The input power of the OTDM data signal is 3 dBm and the pulse width is 2 ps. The channel suppression ratio is the ratio between the minimum of the targeted drop channel and the maximum non-targeted drop channel. The optimum

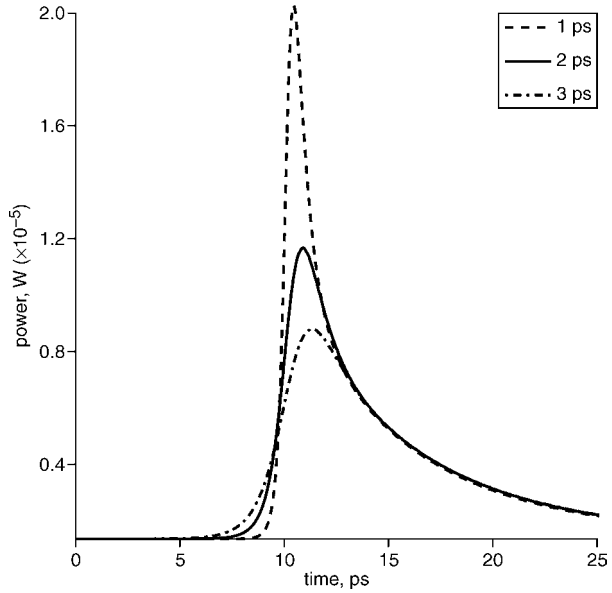

Fig. 3 *The switching windows created with a 1, 2 and 3 ps clock signal. $P_{CW} = 0$ dBm, co-propagating signal and the average power of the clock signal is 10.5 dBm. Length of the active region of the EAM is 150 μm*

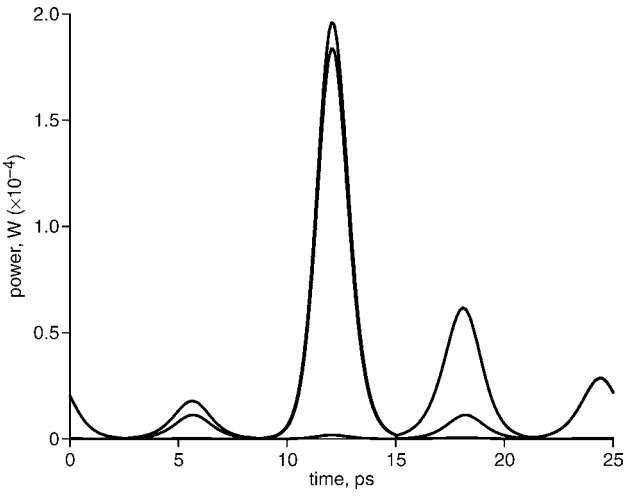

Fig. 4 *Eye diagram of the demultiplexed 40 Gbit/s channel. Clock pulses are 1.6 pJ, which corresponds to a 18 dBm average power*

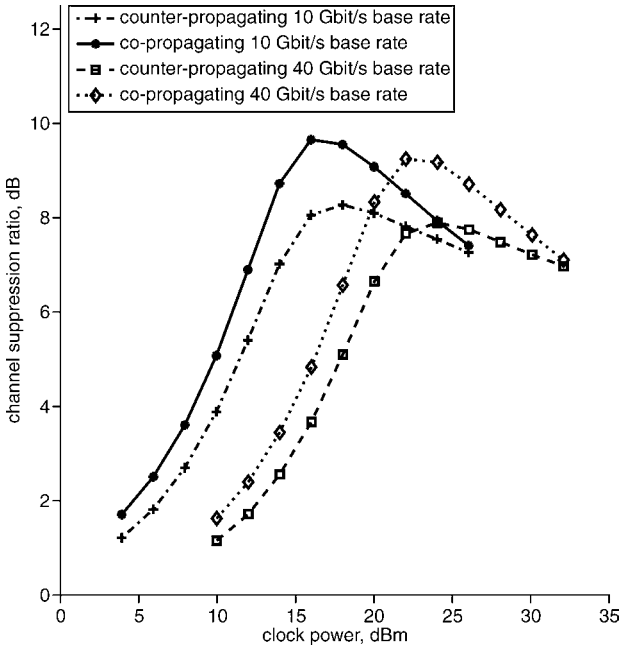

Fig. 5 *Average clock power against the channel suppression ratio. The pulse width of the clock signal is 1.7 ps FWHM. The length of the active region of the EAM is 150 μm*

clock power for both operation modes is around 17 dBm for a 10 Gbit/s base rate and 23 dBm for a 40 Gbit/s base rate. This corresponds to an energy per clock pulse of 5 pJ. This high power is required to bleach the absorption. The channel suppression ratio increases with increasing clock power until a certain optimum value. The decrease of the suppression ratio for a further increase of the input power is caused by the longer recovery time due to a stronger saturation of the absorption. A comparison between co- and counter-propagating operation shows the best performance for co-propagating operation, because of the longer interaction time between the signal and clock pulses. Figure 6 shows the channel suppression ratio for several values of the average clock power as a function of the length of the active region of the EAM for co-propagating operation. Similar results are obtained for counter-propagating operation. As expected, the improvement in the suppression ratio levels out when the power of the clock pulse decreases to a level where the absorption is

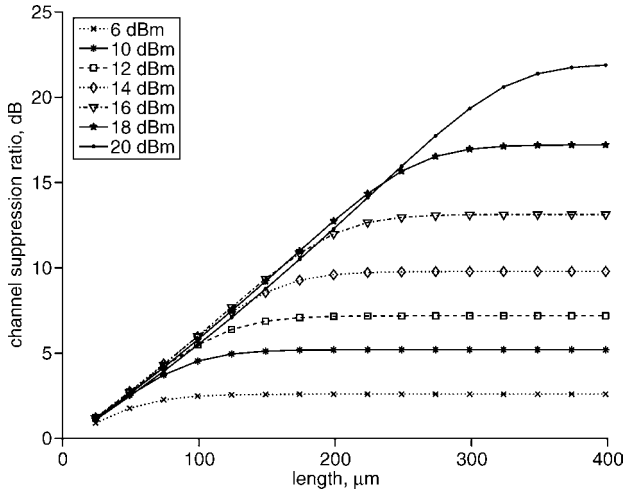

Fig. 6 *The dependence of the channel suppression ratio on the length of the active region of the EAM, for co-propagating operation. The results are shown for different average clock-powers*

no longer influenced. To obtain suppression ratios of 20 dB or higher for co-propagating operation the optimal length of the EAM is larger than 300 μm and the average clock power is 20 dBm or higher.

4 Experimental setup

The experimental setup is shown in Fig. 7. The transmitter consists of a commercial MLL, which generates 2 ps FWHM pulses. A Mach-Zehnder intensity (MZI) modulator operated at 9.9853 Gbit/s with a 2^7-1 pseudo-random bit sequence (PRBS) and a passive delay line multiplexer (MUX) to increase the bit rate to 80 or 160 Gbit/s follows the MLL. The PRBS 2^7-1 is guaranteed up to 40 Gbit/s, but is not maintained for 80 and 160 Gbit/s. The signal is amplified by an erbium-doped fibre amplifier (EDFA) to compensate for the losses in the MZI modulator and the multiplexing stages. A 5 nm optical band-pass filter (OBPF) is used to filter out part of the amplified spontaneous emission (ASE) noise of the EDFA. The clock signal enters the EAM in a counter-propagating direction via the circulator. Counter-propagating operation has been chosen to minimise the chances of damaging the EAM by injecting too much optical power at one of the facets. The gated OTDM channel at the base rate is amplified by another EDFA and filtered with a 3 nm OBPF, before it is sent to the receiver and bit error rate (BER) test set. The other abbreviations and symbols used in Fig. 7 are AM: amplitude modulator, PC: polarisation controller, VA: variable attenuator and τ: optical tuneable delay line. The clock signal is derived from the same MLL source as the OTDM signal. However, to avoid interference between clock and data the wavelength is converted from 1550 to 1540 nm based on supercontinuum generation in 500 metre long HNLF. The experimental setup for this wavelength conversion is shown in Fig. 8. The zero dispersion wavelength of this fibre is $\lambda = 1545$ nm and the dispersion is 0.13 ps/km/nm at 1550 nm, $A_{\text{eff}} = 10.3\ \mu\text{m}^2$ and $\gamma = 15/\text{W/km}$. The average power at the input of the HNLF is 17 dBm. The spectrum of the input pulse is broadened and this so-called super-continuum-generated spectrum is sliced with a 5 nm optical band-pass filter with centre frequency $\lambda_c = 1540$ nm. The FWHM pulse width of the converted clock pulse is measured on the Agilent terascope (bandwidth 500 GHz) and is $\tau_{\text{clock}} = 1.7$ ps, see Fig. 9. The EAM used in the experiments is a commercially available device (OKI), allowing a maximum injected optical power of 13 dBm peak power, which is a limiting factor for the performance of the EAM as an all-optical demultiplexer. Counter-propagating operation is used to minimise the chances of damaging the device due to a high input power. The clock power is step-by-step increased to a maximum value of 12 dBm average power, whereas we would have preferred a higher average input power considering the results of the simulation.

4.1 Switching window

Before looking at the switching window we first took a look at the static characteristics of the EAM, shown in Fig. 10. This Figure indicates that the longer wavelengths, close to the band edge have a relatively small absorption change, due to the relatively low density of states there. On the other hand shorter wavelengths require more energetic pulses to bleach the absorption. Therefore, a trade-off has to be made between the extinction ratio and a reasonable output power. For our OTDM signal we want both a good extinction ratio and a reasonable output power, therefore

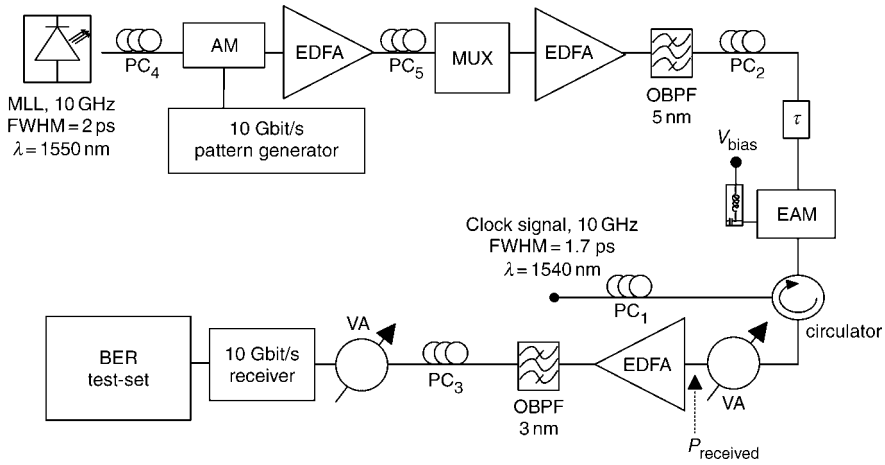

Fig. 7 *Experimental setup for the BER-measurement of the 'all-optical demultiplexer' based on XAM in an EAM*

we chose 1550 nm. For our clock signal we chose 1540 nm. We want this signal to be highly absorbed to have a large influence on the carrier density, creating a gate for the OTDM signal. The switching windows are analysed by injection of a CW at 1550 nm and 2 dBm average power and an optical clock signal at 1540 nm and 10 dBm average power into the EAM. The acquired switching windows are analysed on an Agilent terascope with a 500 GHz bandwidth. The width, rise times and fall times are measured. The relation between the FWHM of the switching window and the reverse bias voltage of the EAM is shown in Fig. 11. A higher reverse bias voltage leads to a faster sweep-out of the photo-generated carriers in the active region of the EAM, because the electrical field working on the carriers is stronger. Therefore, increasing the reverse bias voltage reduces the width of the switching window. The switching window created by XPR + XAM in the EAM is compared with the switching window created by XAM only. The difference in switching

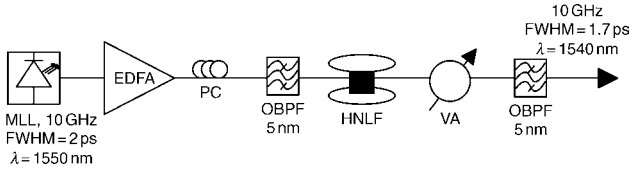

Fig. 8 *Wavelength conversion of the 10 GHz clock signal*

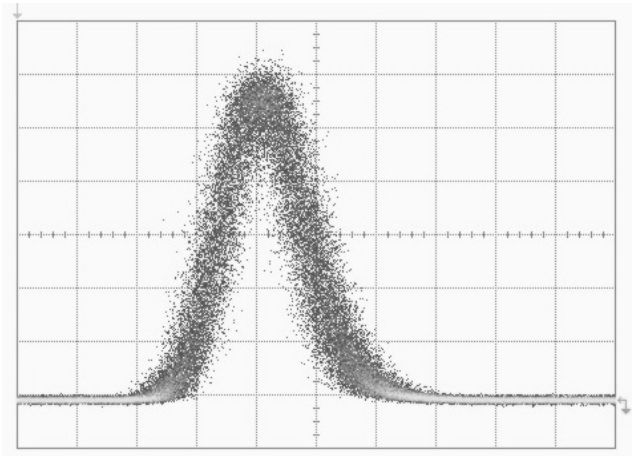

Fig. 9 *Super-continuum-generated pulse at 1540 nm, 1.7 ps FWHM, x-scale: 1 ps/div, y-scale: a.u., measured on the terascope*

window width is circa 1 ps and does not depend on the reverse bias voltage of the EAM. The extinction ratio of the switching window as a function of the reverse bias voltage of the EAM is shown in Fig. 12. The extinction ratio of the switching window created by XPR + XAM has a 1 to 2 dB advantage compared to the switching window created by XAM only. A larger reverse bias voltage leads to a higher extinction ratio of the switching window, which results in a larger channel suppression ratio of the non-targeted channels. The simulations reveal a suppression ratio of 5 dB at a 10 dBm clock power for the length of the active region: $L > 150$ μm. The extinction ratio of the switching window is not exactly the same as the channel suppression ratio. A large tail in the switching window would decrease the channel suppression ratio, but not the extinction ratio of the switching window. Therefore, we have also investigated the tail in the switching window. The total recovery time of the carriers, which corresponds to a tail in the switching window, is equal for the XAM method and the XPR + XAM method. To analyse the tail of the switching window we investigated the fall and rise times on the terascope. The results are shown in Fig. 13. The fall time is defined as the time to go from the 90%-point on the transition to the 10%-point, and the rise time is defined as the time to go from the 10%-point on the transition to the 90%-point. The minimum fall time for XAM and XPR + XAM is respectively 3.2 and 2.5 ps at $V_{EAM} = -3.5$ V. The rise time, however, does not strongly depend on the reverse bias

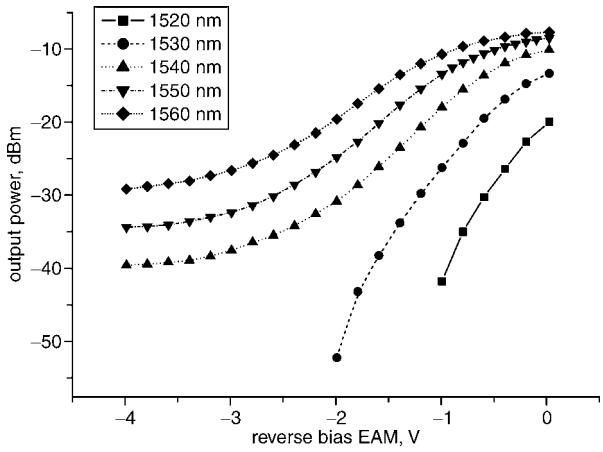

Fig. 10 *Static measurement of CW output power against reverse bias voltage of the EAM for $P_{CWin} = 0$ dBm and $\lambda_{CW} = 1520–1560$ nm*

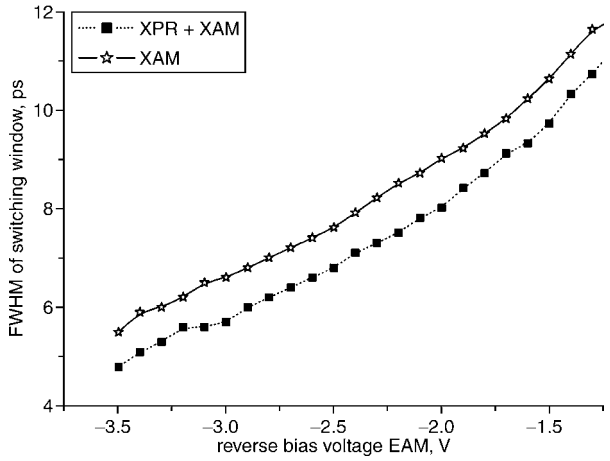

Fig. 11 *Switching window against the reverse bias voltage of the EAM for XAM and XPR + XAM in the EAM*

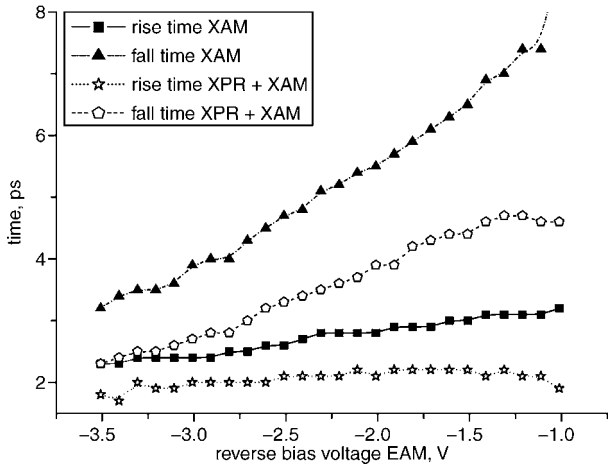

Fig. 13 *Fall and rise times of the switching windows against the reverse bias voltage of the EAM, $P_{CLOCK} = 12$ dBm and $\lambda_{CLOCK} = 1540$ nm, $P_{CW} = 2$ dBm and $\lambda_{CW} = 1550$ nm, measured on the terascope*

voltage of the EAM, as can be seen in Fig. 13. Increasing the speed of operation of the EAM as all-optical switch requires an increase in reverse bias voltage of the EAM. However, the disadvantage is that the absorption in the EAM is also increased and a higher optical power is required to saturate the absorption. Therefore, a careful trade-off has to be made for the optimum reverse bias voltage.

4.2 80 to 10 Gbit/s demultiplexing

For demultiplexing from 80 to 10 Gbit/s we compared the demultiplexed channel with the back-to-back (B2B) signal. Both demultiplexing methods, XAM alone and the combined use of XPR and XAM, are considered. The average input powers coupled into the EAM were $P_{\mathrm{CLOCK}} = 12$ dBm and $P_{\mathrm{OTDM}} = 2$ dBm. After passing through the EAM the signal is first amplified by an EDFA. This is necessary because the EAM is operating in the absorption regime and the received signal power is around -20 dBm. The amplified signal was filtered and attenuated in order not to overload the receiver. During the optimisation of the BER, careful tuning of the bias voltage of the EAM led to best performance at the reverse bias voltage $V_{\mathrm{EAM}} = -1.9$ V. In Fig. 14 the eye-diagrams of the demultiplexed channels for both XAM and XPR + XAM are shown. The difference between the two

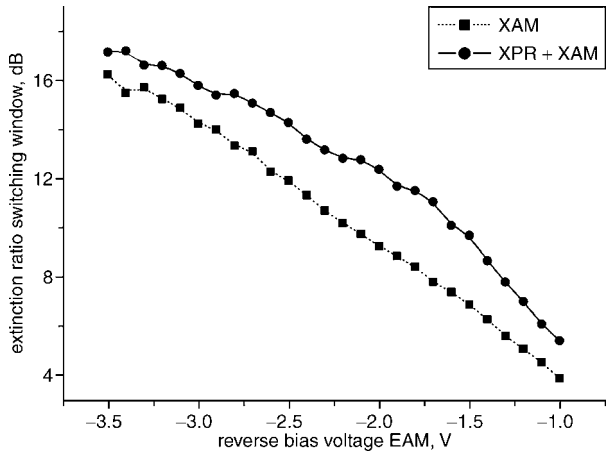

Fig. 12 *Extinction ratio of the switching window against the reverse bias voltage of the EAM for XAM and XPR + XAM in the EAM*

methods is shown in the suppression ratio of the remaining non-targeted channels. Another difference is that the received power for the XPR + XAM method is much lower. As the rotation of the polarisation is about 10° to 15°, a large part of the signal power is blocked at the PBS. The experimental results are compared with the developed simulation model, with input parameters $L = 150$ μm, $P_{\mathrm{CLOCK}} = 12$ dBm, pulse width $T_{\mathrm{CLOCK}} = 1.7$ ps and in counter-propagating operation. The result of this simulation is visualised in Fig. 15. A suppression ratio of about 11 dB of the adjacent channel is obtained in the simulations. This simulation result is very close to the experimentally measured value of 10 dB. Measuring BER values assessed the performance of the all-optical demultiplexer. As a reference for the dropped channels we used the 10 Gbit/s return to zero signal in a B2B BER measurement. Figure 16 summarises the measured BER performances for all eight channels. The average sensitivity penalty for BER of 10^{-9} is 6.7 dB for XPR + XAM and 7.9 dB for XAM. The penalty is due to the ASE noise of the EDFAs and foremost the incomplete removal of the non-targeted channels. Although ASE can be filtered, filtering can never remove the ASE noise that occupies the same spectral region as the signal. If we could increase the clock input power beyond the limit of 13 dBm damage level of the EAM, an improvement of the suppression ratio of the non-targeted channels and a reduction of the sensitivity penalty would be expected.

4.3 160 to 10 Gbit/s demultiplexing

As demultiplexing from 80 to 10 Gbit/s was demonstrated to be error free, the next step is to examine demultiplexing from 160 to 10 Gbit/s. The input powers to the EAM were $P_{\mathrm{CLOCK}} = 12$ dBm and $P_{\mathrm{OTDM}} = 6$ dBm. After passing through the EAM the signal is first amplified by an EDFA. This signal was filtered and attenuated in order not to overload the receiver. During the optimisation of the BER, careful tuning of the bias voltage of the EAM led to best performance at the reverse bias voltage $V_{\mathrm{EAM}} = -2.8$ V. The change in V_{EAM} to a higher reverse bias voltage leads to a faster response time resulting in a smaller switching window. The power of the OTDM input signal injected into the EAM is increased from 2 to 6 dBm to obtain a reasonable signal-to-noise ratio (SNR)

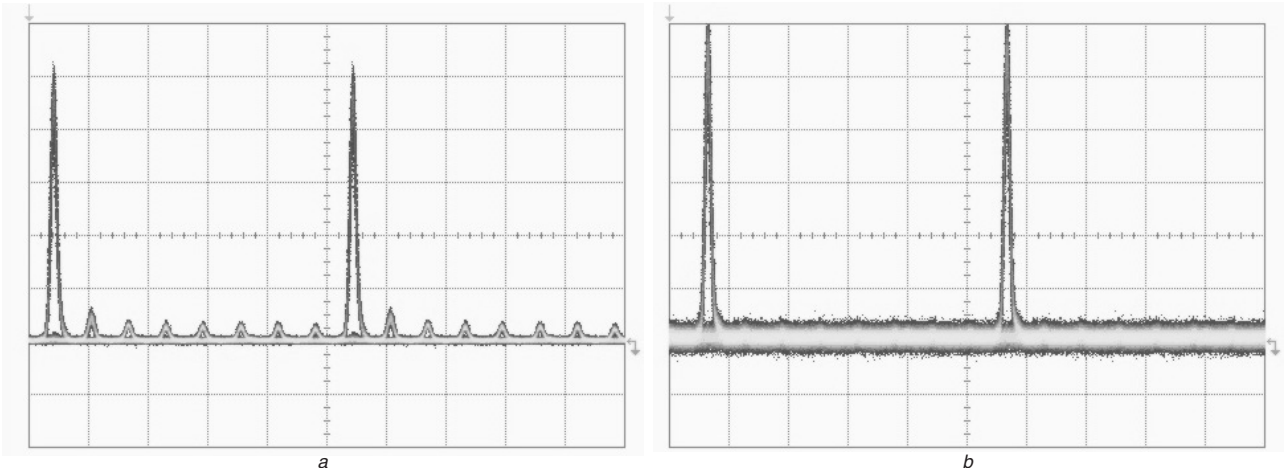

Fig. 14 *The demultiplexed channel from 80 to 10 Gb/s for XAM and for XPR + XAM in the EAM. x-scale: 20 ps/div, y-scale: a.u., measured on the terascope*

a The XAM
b The XPR + XAM

at the output, as the absorption at $V_{EAM} = -2.8$ V is larger than at -1.9 V. The demultiplexed eye-diagrams for XAM and XPR + XAM are shown in Fig. 17. We observed an error floor of 10^{-7}, mainly caused by the insufficiently small switching window. This is indicated by the small suppression ratio of the adjacent channel. The experimental results are compared with the simulation results from the model described in Section 3. The simulation result is visualised in Fig. 18. The suppression of the adjacent channel in the simulations is 5.3 dB. The simulations are in good agreement with the experimental results. If we could increase the input power beyond the 13 dBm damage level to about 17 dBm higher suppression ratios of non-targeted channels can be expected. We expect based on the results obtained from our simulation model that an increase of the input power will lead to error-free demultiplexing. Although a small penalty for the insufficiently small switching window is still expected.

5 Discussion and Conclusions

We have performed a comprehensive study on XAM in an EAM. A model based on propagation equations to simulate the XAM in the EAM has been developed. The model includes an absorption coefficient, which is calculated based on a function of carrier distributions in the active region and the effects of SHB and carrier cooling are also taken into account. We showed good agreement between the experimental results and the theoretical model of the EAM. We have demonstrated error-free demultiplexing from 80 to 10 Gbit/s based on XAM in a commercially available EAM. We also introduced the concept of XPR to increase the extinction ratio of the XAM-based demultiplexer. However, we did not observe a significant improvement by using XPR, only a 1.2 dB sensitivity improvement is observed. In addition, it introduces polarisation sensitivity to the demultiplexing configuration. Furthermore, we have investigated the feasibility of using this method at 160 Gbit/s.

The performance of the EAM as an all-optical demultiplexer is strongly dependent on the maximum non-destructive input power. With a higher clock power the saturation effect of the absorption will be stronger. Stronger absorption saturation leads also to an increased induced birefringence change resulting in a larger rotation of the polarisation. The operation speed of the EAM as demultiplexer in an all-optical configuration is limited by the carrier recovery time. Increasing the reverse bias voltage shortens the recovery time. However, this leads to an increase in absorption, which requires a higher input power to saturate the absorption, otherwise degradation of the SNR is unavoidable. In [9] demultiplexing from 160

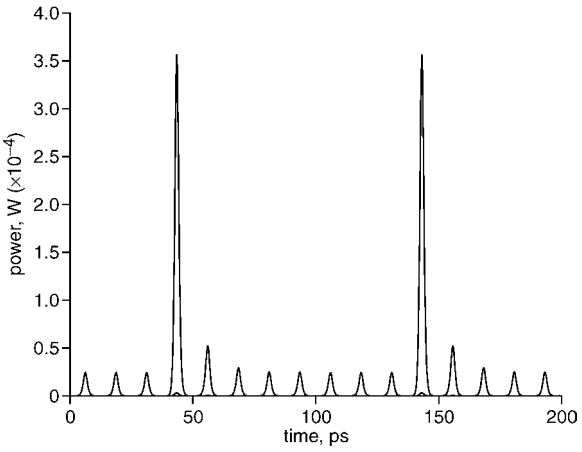

Fig. 15 *Simulation result of demultiplexing from 80 to 10 Gbit/s based on XAM*

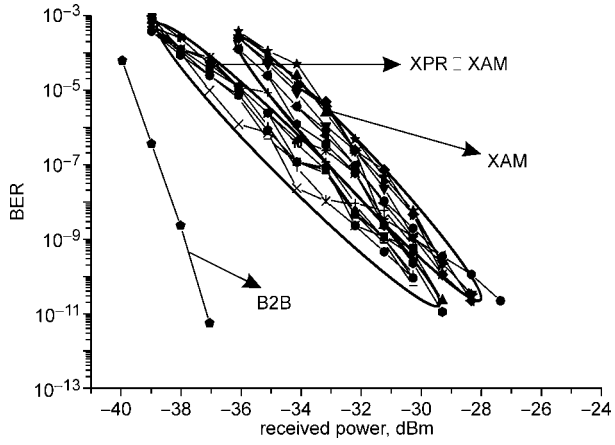

Fig. 16 *The BER performance of demultiplexing from 80 to 10 Gbit/s for all the eight channels based on XPR + XAM and XAM compared to the B2B measurement*

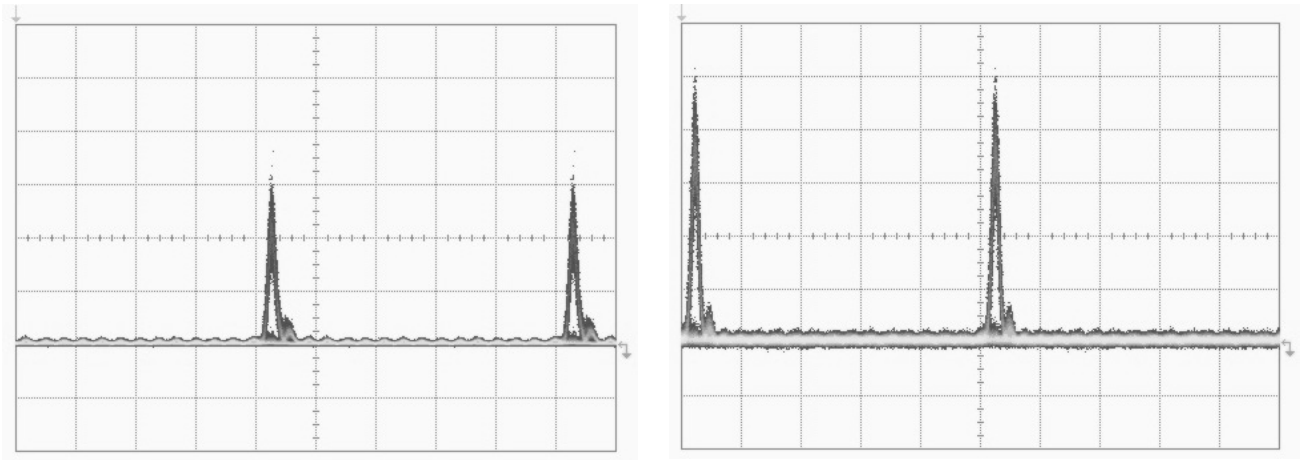

a b

Fig. 17 *The demultiplexed channel from 160 Gbit/s to 10 Gbit/s for XAM and for XPR + XAM in the EAM. x-scale: 20 ps/div, y-scale: a.u., measured on the terascope*

a The XAM
b The XPR + XAM

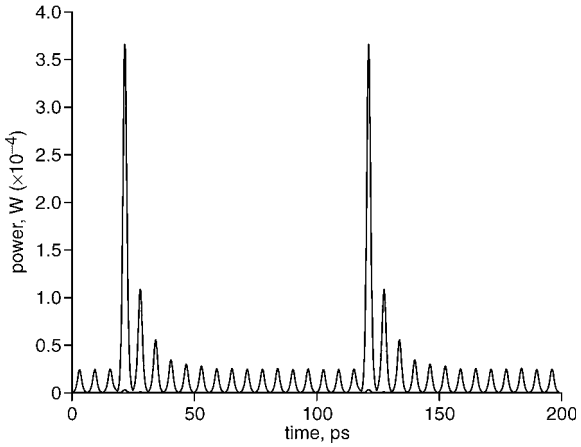

Fig. 18 *Simulation result of demultiplexing from 160 to 10 Gbit/s based on XAM*

to 10 Gbit/s in co-propagating operation has been shown using a 16.3 dBm average control power, with a XAM optimised EAM structure. The requirement for a high input power is also expected from our simulation model; however, we were severely limited by the maximum non-destructible input power of the commercially available EAM, besides our EAM is optimised for external modulation and not for XAM. All-optical demultiplexing with the available EAM and the limit of 13 dBm input power has limited us to demultiplexing from 160 to 10 Gbit/s with an error floor of about 10^{-7}. When there is a 40 GHz RF signal available a suitable 160 to 40 add-drop multiplexing [25] with travelling wave EAMs has been shown feasible.

6 Acknowledgment

This research was supported by the Towards Freeband Communication Impulse of the technology programme of the Ministry of Economic Affairs of The Netherlands.

7 References

1 Spirit, D.M., Ellis, A.D., and Barnsley, P.E.: 'Optical time division multiplexing: Systems and Networks', *IEEE Commun. Mag.*, 1994, **32**, (12), pp. 56–62
2 Li, J., Olsson, B.-E., Karlsson, M., and Andrekson, P.A.: 'OTDM demultiplexer based on XPM-induced wavelength shifting in highly nonlinear fiber', *IEEE Photonics Technol. Lett.*, 2003, **15**, (12), pp. 1770–1772
3 Morioka, T., Takara, H., Kawanishi, S., Kitoh, T., and Saruwatari, M.: 'Error-free 500 Gbit/s all-optical demultiplexing using low-noise, low-jitter supercontinuum short pulses', *Electron. Lett.*, 1996, **32**, (9), pp. 833–834
4 Jansen, S.L., Heid, M., Spalter, S., Meissner, E., Weiske, C.J., Schopflin, A., Khoe, D., and de Waardt, H.: 'Demultiplexing 160 Gbit/s OTDM signal to 40 Gbit/s by FWM in SOA', *Electron. Lett.*, 2002, **38**, (17), pp. 978–980
5 Schubert, C., Berger, J., Diez, S., Ehrke, H.J., Ludwig, R., Feiste, U., Schmidt, C., Weber, H.G., Toptchiyski, G., Randel, S., and Petermann, K.: 'Comparison of interferometric all-optical switches for demultiplexing applications in high-speed OTDM systems', *J. Lightwave Technol.*, 2002, **20**, (4), pp. 618–624
6 Sokoloff, J., Pruncnal, P., Glesk, I., and Klane, M.: 'A terahertz optical asymmetric demultiplexer (TOAD)', *IEEE Photonics Technol. Lett.*, 1993, **5**, (7), pp. 787–790
7 Turkiewicz, J.P., Tangdiongga, E., Rohde, H., Schairer, W., Lehmann, G., Khoe, G.D., and de Waardt, H.: 'Simultaneous high speed OTDM add-drop multiplexing using GT-UNI switch', *Electron. Lett.*, 2003, **39**, (10), pp. 795–796
8 Schubert, C., Schmidt, C., Ferber, S., Ludwig, R., and Weber, H.G.: 'Error-free all-optical add-drop multiplexing at 160 Gbit/s', *Electron. Lett.*, 2003, **39**, (14), pp. 1074–1076
9 Xu, L., Chi, N., Christiansen, L.J., Yvind, K., Oxenløwe, L.K., Mørk, J., and Jeppesen, P.: '160 to 10 Gbit/s all-optical demultiplexing using a single electroabsorption modulator'. Presented at the 30th European Conf. on Optical Communication, Stockholm, Sweden, 2004, paper We 1.5.3
10 Chou, H.-F., Chiu, Y.-J., Wang, W., Bowers, J.E., and Blumenthal, D.J.: 'Compact 160-Gbit/s demultiplexer using a single-stage electrically gated electroabsorption modulator', *IEEE Photonics Technol. Lett.*, 2003, **15**, (10), pp. 1458–1460
11 Kodama, S., Yoshimatsu, T., and Ito, H.: '320 Gbit/s error-free demultiplexing using ultrafast optical gate monolithically integrating a photodiode and electroabsorption modulator', *Electron. Lett.*, 2003, **39**, (17), pp. 1269–1270
12 Chou, H.-F., Chiu, Y.-J., and Bowers, J.E.: 'Standing-wave enhanced electroabsorption modulator for 40-GHz optical pulse generation', *IEEE Photonics Technol. Lett.*, 2003, **15**, (2), pp. 215–217
13 Nishimura, K., Inohara, R., Tsurusawa, M., and Usami, M.: '80 Gbit/s wavelength conversion using MQW electroabsorption modulator in delayed-interferometric configuration', *Electron. Lett.*, 2003, **39**, (10), pp. 792–793
14 Boerner, C., Schubert, C., Schmidt, C., Hilliger, E., Marembert, V., Berger, J., Ferber, S., Dietrich, E., Ludwig, R., Schmauss, B., and Weber, H.G.: '160 Gbit/s clock recovery with electro-optical PLL using bidirectionally operated electroabsorption modulator as phase comparator', *Electron. Lett.*, 2003, **39**, (14), pp. 1071–1073

15 Awad, E.S., Cho, P.S., Moulton, N., and Goldhar, J.: 'Subharmonic optical clock recovery from 160 Gbit/s using time-dependent loss saturation inside a single electroabsorption modulator', *IEEE Photonics Technol. Lett.*, 2003, **15**, (12), pp. 1764–1766
16 Turkiewicz, J.P., Tangdiongga, E., Khoe, G.D., and de Waardt, H.: 'Clock recovery and demultiplexing performance of 160-gb/s OTDM field experiments', *IEEE Photonics Technol. Lett.*, 2004, **16**, (2), pp. 611–613
17 Schuh, K., Schmidt, M., Lach, E., Junginger, B., Klekamp, A., Veith, G., and Sillard, P.: '4 × 160 Gbit/s DWDM/OTDM transmission over 3 × 80 km Teralight™–Reverse TeraLight™ fibre'. Presented at the 28th European Conf. on Optical Communication, Copenhagen, Denmark, 2002, paper 2.1.2.
18 Awad, E.S., Cho, P.S., Moulton, N., and Goldhar, J.: 'All-optical timing extraction with simultaneous optical demultiplexing from 40 Gbit/s using a single electroabsorption modulator', *IEEE Photonics Technol. Lett.*, 2003, **15**, (1), pp. 126–128
19 Ohno, T., Iga, R., Kondo, Y., Ito, T., Furuta, T., Yoshino, K., Ito, H., and Sato, K.: 'Wide-locking-range 160-GHz optical clock recovery from 160-Gbit/s signal using a mode-locked laser diode'. Presented at the Optical Fiber Communication Conf., Los Angeles, CA, USA, 2004, paper WD-5
20 Oxenløwe, L.K., Romstad, F., Tersigni, A., Hojfeldt, S., Yvind, K., Skovgaard, P.M.W., Hoppe, K., and Hanberg, J.: 'Characterization of a MQW electroabsorption modulator as an all-optical demultiplexer'. Proc. 14th Annual Meeting of the IEEE Lasers and Electro-Optics Society, San Diego, CA, USA, 2001, Vol. 1, pp. 36–37
21 Verdurmen, E.J.M., Heck, M., Khoe, G.D., and de Waardt, H.: 'Modelling and study of all-optical demultiplexing of a 160 Gbit/s OTDM signal using a QW-EAM'. Proc. IEEE Lasers and Electro Optics Society (LEOS), Benelux, Enschede, The Netherlands, 2003, pp. 161–164
22 Liu, Y., Turkiewicz, J.P., Verdurmen, E.J.M., de Waardt, H., Khoe, G.D., and Dorren, H.J.S.: 'All-optical wavelength conversion by utilizing cross-polarization modulation in an electro-absorption modulator'. Presented at the 29th European Conf. on Optical Communication, Rimini, Italy, 2003, paper We4.P78
23 Uskov, A.V., Karin, J.R., Bowers, J.E., McInerney, J.G., and Bihan, J.L.: 'Effects of carrier cooling and carrier heating in saturation dynamics and pulse propagation through bulk semiconductor absorbers', *IEEE J. Quantum Electron.*, 1998, **34**, (11), pp. 2162–217
24 Højfeldt, S.: 'Modeling of carrier dynamics in electroabsorption modulators'. PhD Thesis, COM Technical University of Denmark, May 2002
25 Chou, H.-F., Bowers, J.E., and Blumenthal, D.J.: 'Compact 160-Gbit/s add-drop multiplexer with a 40-Gbit/s base rate using electroabsorption modulators', *IEEE Photonics Technol. Lett.*, 2004, **16**, (6), pp. 1564–1566